

In the format provided by the authors and unedited.

A scalable multi-photon coincidence detector based on superconducting nanowires

Di Zhu¹, Qing-Yuan Zhao^{1,2*}, Hyeongrak Choi¹, Tsung-Ju Lu¹, Andrew E. Dane¹, Dirk Englund¹ and Karl K. Berggren^{1*}

¹Research Laboratory of Electronics, Massachusetts Institute of Technology, Cambridge, MA, USA. ²Research Institute of Superconductor Electronics, School of Electronic Science and Engineering, Nanjing University, Nanjing, Jiangsu, China. *e-mail: qyzhao@nju.edu.cn; berggren@mit.edu

CONTENTS

I. Device fabrication	3
II. Basic detector metrics of the 16-element device	5
A. Detector efficiency and dark count rate	5
B. Timing jitter	5
C. Maximum count rate	6
III. Supplementary figures for the 4-element device	8
A. Counting ratio and laser pulse width estimation	8
B. Complete list of all pulse shapes and their fingerprints	9
IV. Discussion on waveguide integration	13
References	14

I. DEVICE FABRICATION

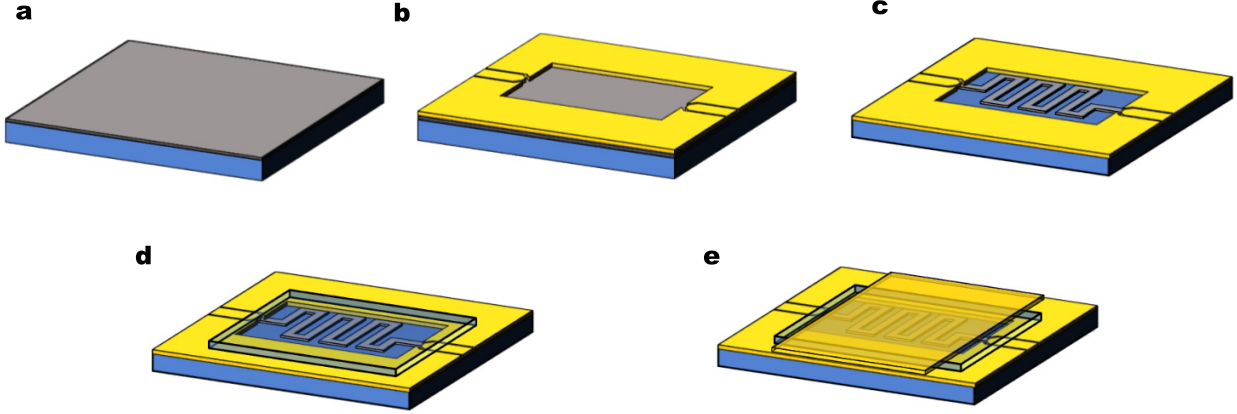


FIG. S1. Fabrication process. **a**, NbN deposition on an **AlN-on-sapphire substrate**. The NbN film was deposited using DC magnetron sputtering at 840 °C¹. **b**, Gold pad fabrication. The bottom electrical contact pads and alignment marks were defined using contact photolithography. A bilayer resist with PMGI SF9 and S1813 were used to facilitate lift-off. The metal (5 nm Ti/50 nm Au/5 nm Ti) were deposited using electron-beam evaporation. **c**, Nanowire patterning. The superconducting nanowires were patterned using electron-beam lithography (EBL). 4% HSQ was spin coated to the sample at 4 krpm for 1 min. A 125 keV EBL system (Elionix F125) was used to expose the resist. The beam current was 1 nA, and the dose was 3840 $\mu\text{C}/\text{cm}^2$. The HSQ was developed in 25% TMAH for 2 min and rinsed with DI water. The HSQ pattern was transferred to the NbN film using reactive ion etching with CF₄ chemistry (He:CF₄ 7 sccm: 15 sccm). The etching was at 10 mTorr, 50 W for 1 min 45 s. **d**, Dielectric spacer fabrication. Dow Corning FOX-16 was spin coated at 3 krpm for 1 min and baked at 250 °C for 2 min. The intended area was exposed using EBL at 20 nA with a dose of 800 $\mu\text{C}/\text{cm}^2$, then developed in CD-26 for 70 s followed by rinsing in DI water. We measured the thickness of the spacer to be 450 nm using a surface profiler (Dektak). **e**, Top grounding plane fabrication. The top grounding plane was fabricated using a similar process as **b**. It was designed to extend outside the dielectric spacer to make a contact to the bottom common ground.

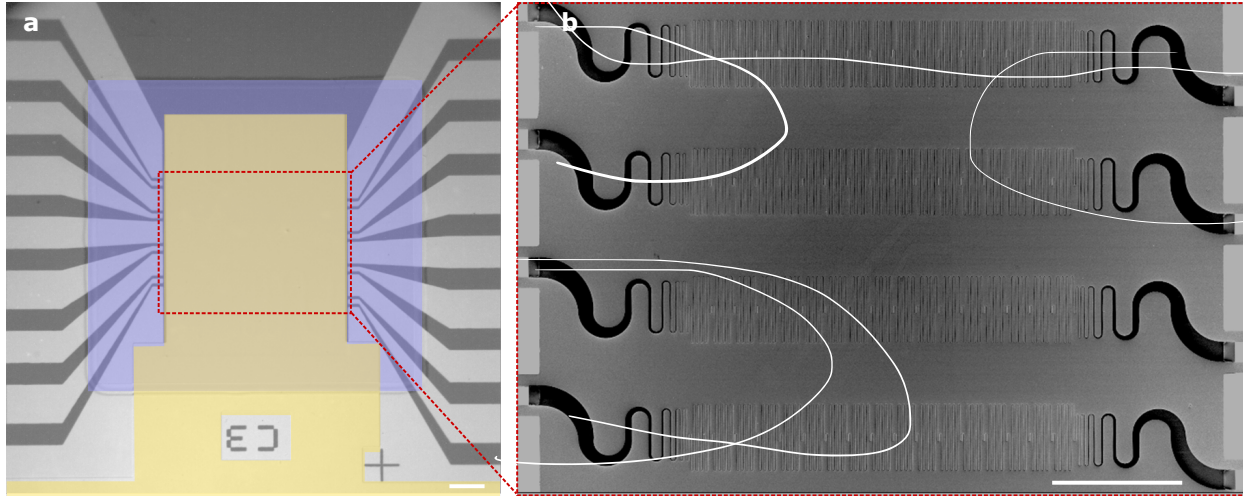


FIG. S2. Micrographs of the fabricated device. **a**, Optical micrograph of the final fabricated device. The light gray area on the bottom is the gold contact pads, and the dark gray area is the substrate. The purple area marks the middle dielectric spacer. The yellow area marks the top gold grounding plane. The red box at the center marks the actual location of the superconducting nanowire. **b**, Scanning electron micrograph of the superconducting nanowires before putting on the dielectric spacer and top ground. 4 sets of detectors were fabricated in the same device area. Scale bar: 100 μm .

II. BASIC DETECTOR METRICS OF THE 16-ELEMENT DEVICE

A. Detector efficiency and dark count rate

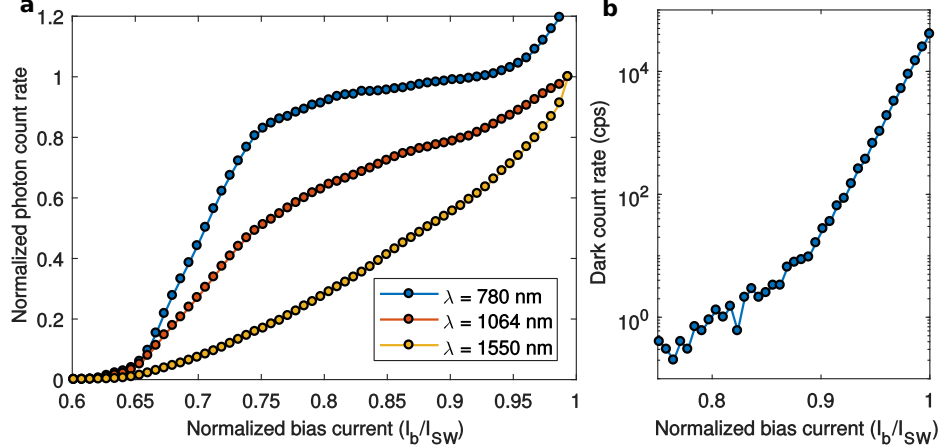


FIG. S3. Detector efficiency and dark count in the 16-element detector

a, Normalized photon count rate (PCR) vs. normalized bias current under different photon energies. The PCR for 1064 nm and 1550 nm was normalized to their maximum count rates, while the PCR for 780 nm were normalized to the “plateau” region, and the value was chosen to be the average of the points near minimum $\frac{dPCR}{dI_b}$. At 780 nm illumination, the count rate was saturated, indicating high internal quantum efficiency. The increased photon count rate near I_{SW} at 780 nm may be due to (1) triggering of the delay line by the high energy photons when flood illuminated, (2) capacitive charging of the AC coupled amplifier at high count rate which increases the effective bias², or (3) increased dark count rate under illumination which in turn increases measured photon count rate³.

b, Dark count rate vs. normalized bias current.

B. Timing jitter

Fig. S4 shows the distribution of t_{sum} in the 16-element detector measured using a 1550 nm sub-ps pulsed laser in the single-photon regime, showing a FWHM sum jitter of 59 ps.

Device timing jitter, together with uncertainty of photon arrival time with respect to the reference clock, determine the minimum delay line required to resolve all the detection events. In the main text, we showed that the 4-element device had a FWHM difference jitter of 20 ps and sum jitter of 56 ps. For the 16-element device, the FWHM difference jitter

was also 20 ps and the sum jitter was 59 ps (see Fig. S4). This increased sum jitter was likely due to the variation in pulse shapes caused by imperfect impedance matching. The variation in pulse shape, especially on the rising edge, will induce fluctuation of triggering point for time tagging. Given these values, We estimated $\sigma_e = 20/2.355 = 8.5$ ps and $\sigma_{\text{det}} = (59^2 - 20^2)^{1/2}/2.355 = 23.6$ ps. Based on the current timing jitter, for example, to resolve a pulsed spontaneous parametric down-conversion photon pair that has a FWHM timing uncertainty of 2 ps with respect to the timing reference given by the pump laser⁴, we would need a delay line of 150.6 ps (6σ) to achieve >99.7% fidelity.

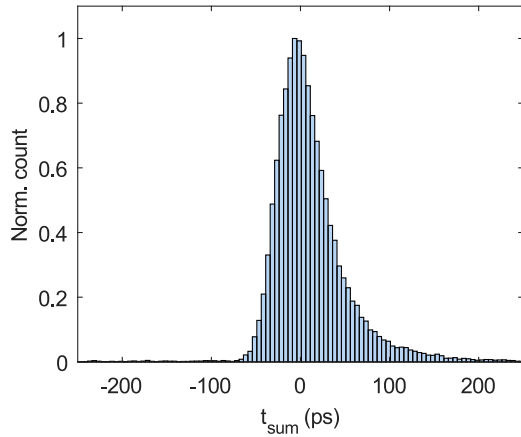


FIG. S4. Sum jitter for the 16-element device. The t_{sum} was measured using the 1550 nm sub-ps laser in the single-photon regime. The measured FWHM sum jitter was 59 ps, which was higher than that in the 4-element detector (56 ps). The increased jitter was likely due to the larger variation in pulse shapes (16 different pulse shapes), which causes fluctuation in triggering point during time tagging.

C. Maximum count rate

Figure S5 shows the count rate measurement of the 16-element detector. At 3 dB efficiency suppression point, the maximum count rate was 4.8 MHz.

The reset time of the detector is limited by the kinetic inductance of the nanowire⁵. The maximum count rate can be roughly estimated as $R_{\text{load}}/[3N(L_{\text{det}} + L_{\text{delay}})] = O(1/N)$, where N is the number of segments, L_{load} is the load impedance (50 Ω in our case), L_{det} and L_{delay} are the inductance for each detector segment and each delay line.

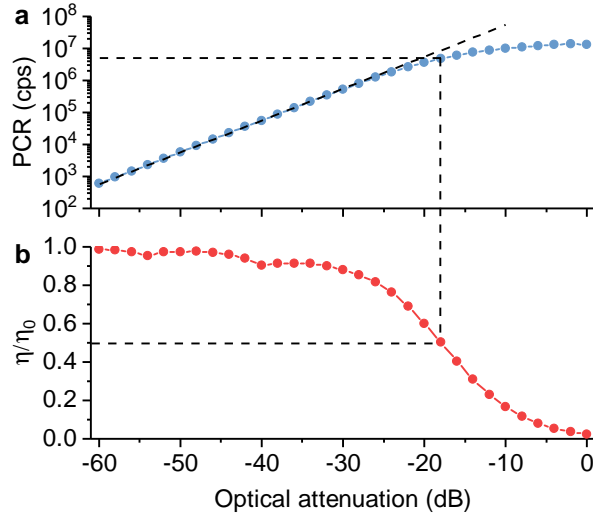


FIG. S5. Maximum count rate of the 16-element detector. **a**, Measured photon count rate (subtracted dark count rate) as a function of optical attenuation. **b**, Normalized detection efficiency as a function of optical attenuation. The maximum count rate was measured to be 4.8 MHz at the 3 dB suppression point for the detection efficiency. The light source was a superluminescent diode with a center wavelength at 1550 nm. We used the setup described in Ref. 6 to avoid capacitive charging at the amplifier.

III. SUPPLEMENTARY FIGURES FOR THE 4-ELEMENT DEVICE

A. Counting ratio and laser pulse width estimation

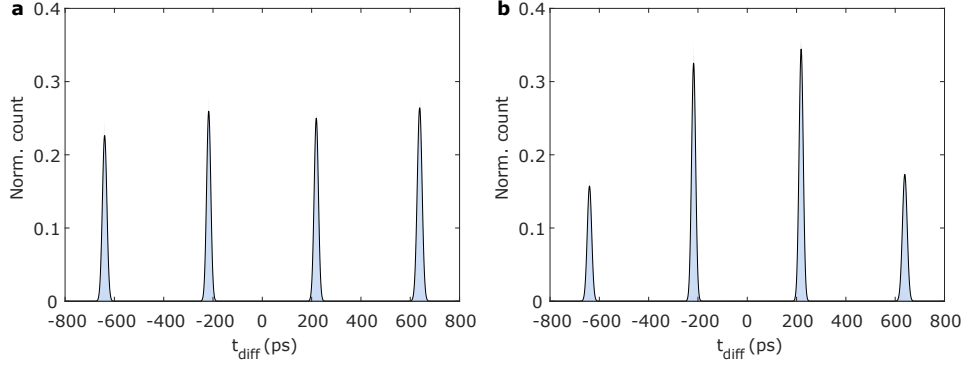


FIG. S6. Counting rate distribution in the 4-element detector. **a**, When the probing fiber was far away from the detector, all the segments were illuminated uniformly, and they have a relatively uniform counting rate with a ratio of [0.2263, 0.2595, 0.2500, 0.2642]. **b**, When the fiber was focused at the center of the detector, the middle two segments had a higher counting rate, and the counting ratio was [0.1573, 0.3252, 0.3443, 0.1732]. This ratio was used as c_i in the photon statistics modeling.

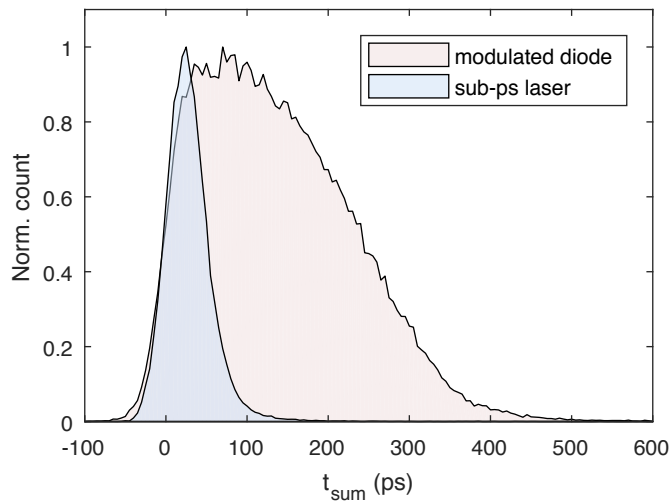


FIG. S7. Laser pulse shape comparison. The FWHM sum jitter was 50 ps when illuminated using the sub-ps laser, while it was 240 ps when illuminated using the modulated diode laser.

B. Complete list of all pulse shapes and their fingerprints

In this section, we show a complete list of all 15 observed pulse shapes from the 4-element array, including 4 single-photon events, 6 two-photon events, 4 three-photon events, and 1 four-photon event. The 4-element array was illuminated using a modulated diode laser, which introduced a photon-arrival jitter of ~ 200 ps.

Fig. S8 shows the averaged pulse shapes. As we can see, many pulses share the same rising edges (i.e. giving the same time tags), but start to diverge after about 400 ps to a few ns. This time scale is close to the delay time between adjacent detecting elements (426 ps), and is consistent with our hypothesis that the distinct pulse shapes from different detection events were caused by reflections from the hotspots and terminals in the nanowire. Moreover, the pulse shapes deviate further after more reflections, forming distinct ripples in the falling edge.

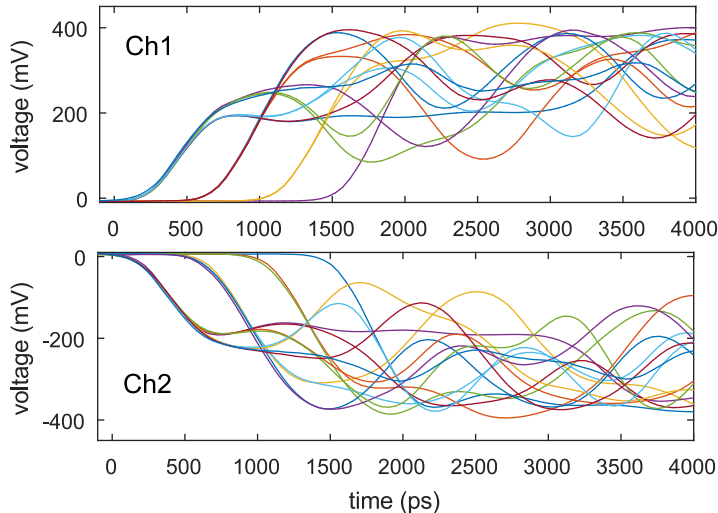


FIG. S8. Averaged pulse shapes for all detection cases measured in the 4-element array. The upper panel shows the output pulses from Ch1, and the lower panel shows the output pulses from Ch2, which has the opposite polarity.

We separated the observed pulse shapes into 4 categories: (1) single-photon events (Fig. S9), where only 1 detector fires; (2) unambiguous two-photon events (Fig. S10), where 2 adjacent detectors fire; (3) ambiguous two-photon events (Fig. S11), where a detector and its next-nearest neighbor fire, leaving an ambiguity of whether the middle detector fires; and

(4) ambiguous two, three, and four-photon events (Fig. S12), where D_1 and D_4 fire, leaving four possible situations (D_1D_4 , $D_1D_2D_4$, $D_1D_3D_4$, and $D_1D_2D_3D_4$).

Different from the clean averaged pulse shapes shown in Fig. S8, the single-shot waveforms present more variation and noise. In the current measurement, the variation was primarily due to the photon arrival jitter. Given the 200-ps pulse width, when multiple detectors fire, the hotspot formation/growth in one detector could delay another by as long as 200-ps. This variation can be seen in the jitter of the rising edge. More importantly, this initial time variation will further affect the reflection dynamics in the nanowire, especially when the two detectors are nearby. When the photon-arrival jitter is low, other effects, such as the avalanche process in the SNAP^{7,8} or multiphoton absorption on the same pixel⁹, may also lead to variations in the output pulses.

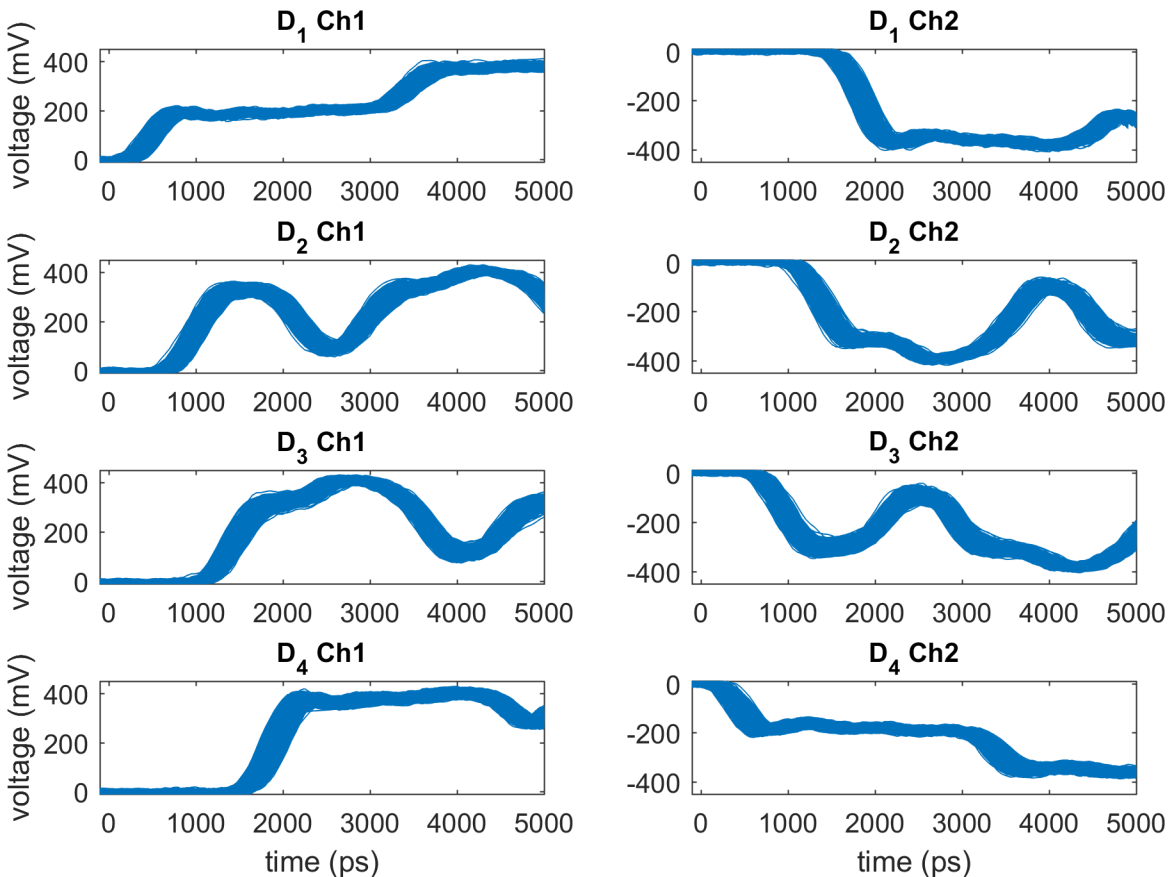


FIG. S9. Detector pulses for all single-photon cases. Left panels show output pulses from Ch1, and the right panels show output pulses from Ch2, which have opposite polarities.

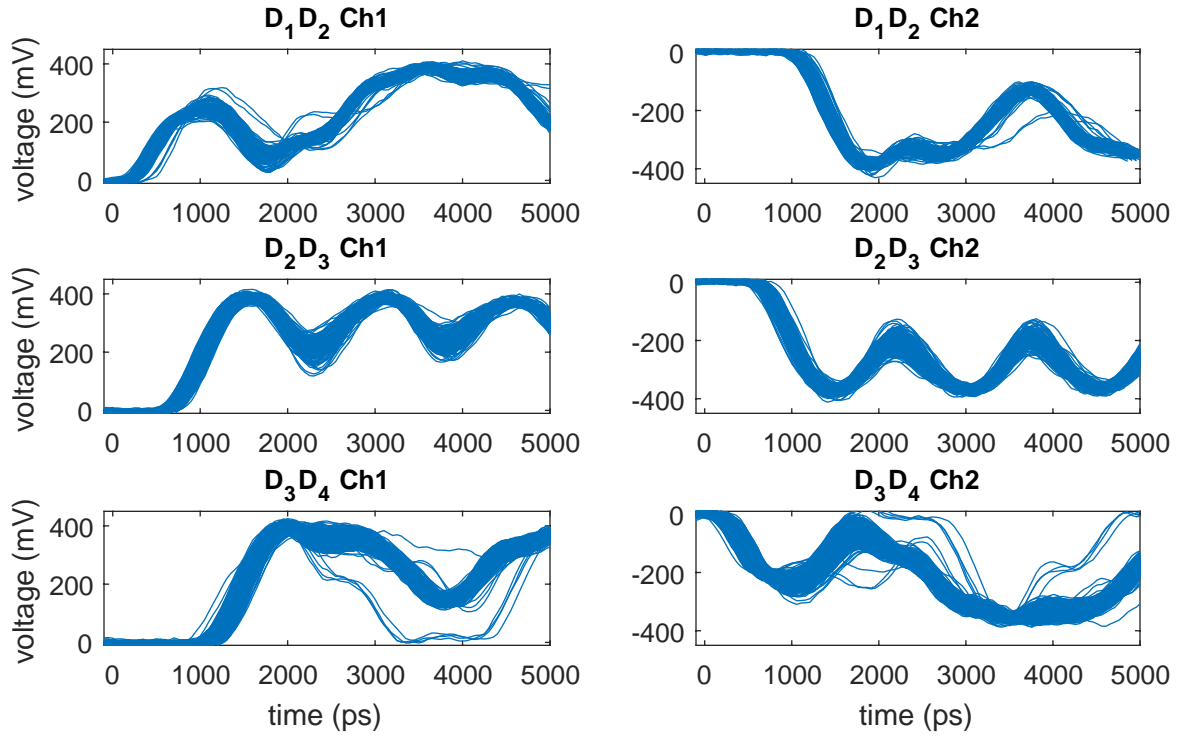


FIG. S10. Detector pulses for unambiguous two-photon events. These two-photon detection events originated from adjacent detectors. In these cases, the timing logic on its own was sufficient to determine which two detecting elements fired without ambiguity, since no detecting elements in between could fire. We noticed some irregular pulse shapes for D_1D_2 and D_3D_4 events, but the reason was not completely understood yet.

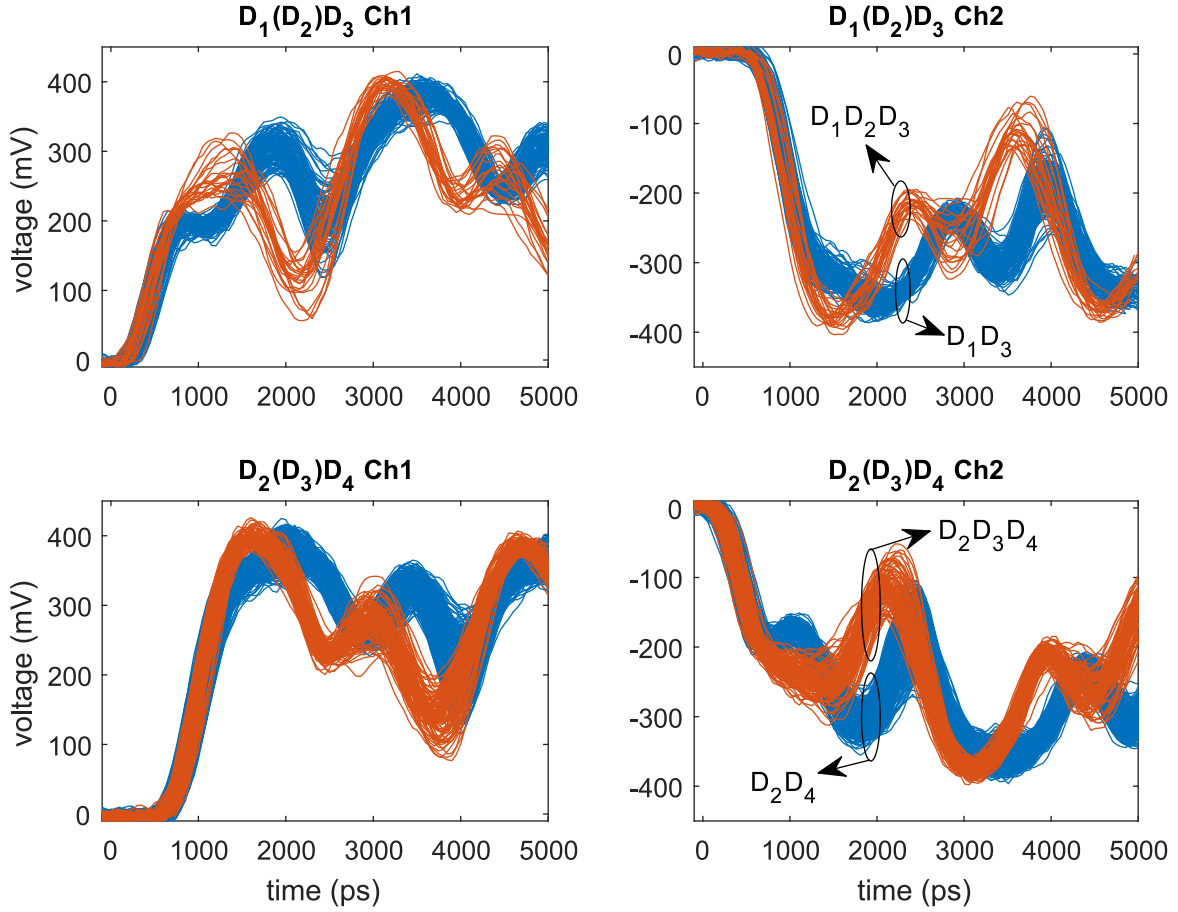


FIG. S11. **Detector pulses for ambiguous two-photon events.** The circles indicate the fingerprints used to distinguish the events.

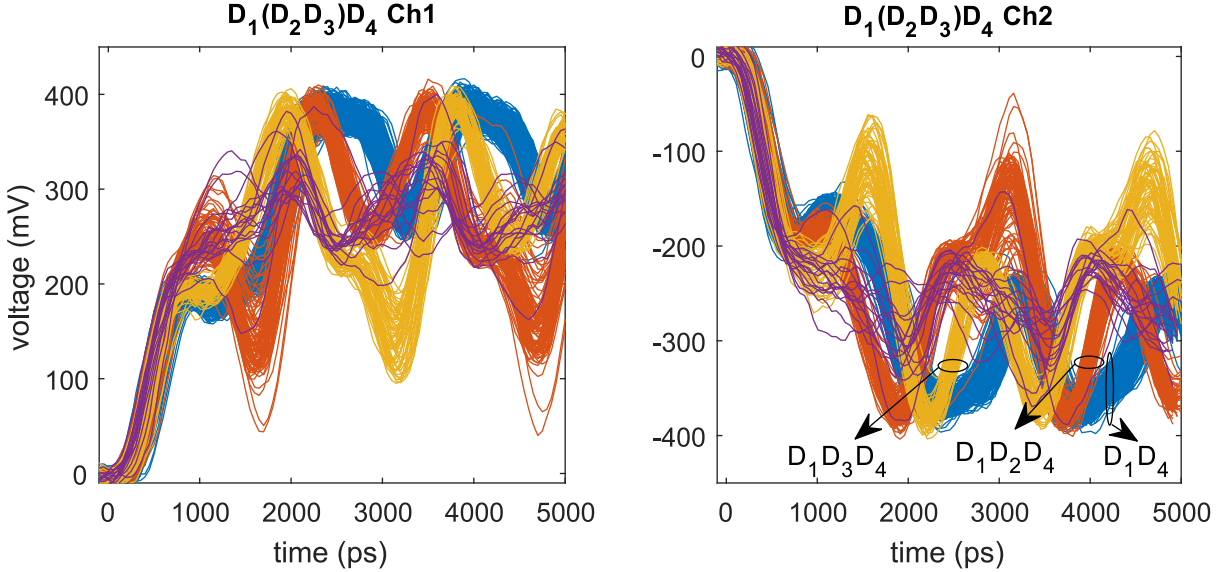


FIG. S12. **Detector pulses for ambiguous two, three, and four events.** The circles indicate the fingerprints used to distinguish the events. We counted $D_1D_2D_3D_4$ events (purple) by identifying pulses that do not match the other three fingerprints.

IV. DISCUSSION ON WAVEGUIDE INTEGRATION

The detection efficiency is the product of the internal quantum efficiency (η_{int}) and optical absorption (η_{abs}). The optical absorption can in principle reach unity when the detector is integrated on an optical waveguide^{10,11}. Simply etching the AlN substrate into a 450 nm × 200 nm ridge waveguide, the 80-nm-wide 2-SNAP will have an absorption rate of 1.15 dB/μm for the transverse electric (TE) mode at 637 nm wavelength, which corresponds to the zero-phonon line of nitrogen vacancy centers in diamond. Figure S13 shows the numerical simulation for the waveguide mode and absorption rate. To achieve >90% absorption, the 2-SNAP needs to be 8.7 μm long. Adding a reflector or photonic crystal cavity on the waveguide can further reduce the length¹². The ability to control absorption by changing the nanowire length can be used to cascade multiple partially absorbing detector chains in parallel on an optical waveguide array. This method can be used to handle input states with more than two photons or resolving multi-photons in the same mode/waveguide.

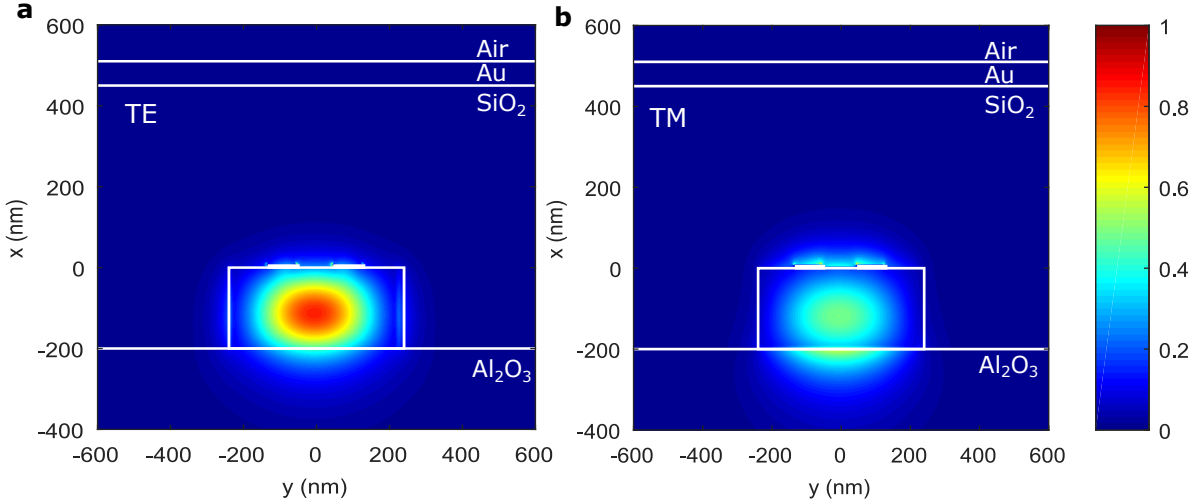


FIG. S13. Calculation of the optical absorption in the superconducting nanowire when integrated on waveguide. The mode pattern (normalized $|\mathbf{E}|^2$) for a $450 \text{ nm} \times 200 \text{ nm}$ AlN waveguide with integrated 2-SNAPs at 637 nm wavelength. **a**, Transverse electric mode. $n_{\text{eff}} = 1.86 + 0.0134i$, and absorption rate is $1.146 \text{ dB}/\mu\text{m}$. **b**, Transverse magnetic mode. $n_{\text{eff}} = 1.83 + 0.0085i$, and absorption rate is $0.73 \text{ dB}/\mu\text{m}$. The simulation was performed using Lumerical MODE Solutions.

REFERENCES

- ¹Najafi, F. *et al.* Fabrication process yielding saturated nanowire single-photon detectors with 24-ps jitter. *IEEE J. Sel. Top. Quantum Electron.* **21**, 1–7 (2015).
- ²Kerman, A. J., Rosenberg, D., Molnar, R. J. & Dauler, E. A. Readout of superconducting nanowire single-photon detectors at high count rates. *J. Appl. Phys.* **113**, 144511 (2013).
- ³Chen, S. *et al.* Dark counts of superconducting nanowire single-photon detector under illumination. *Opt. Express* **23**, 10786 (2015).
- ⁴Chen, C. *et al.* Efficient generation and characterization of spectrally factorable biphotons. *Opt. Express* **25**, 7300 (2017).
- ⁵Kerman, A. J. *et al.* Kinetic-inductance-limited reset time of superconducting nanowire photon counters. *Appl. Phys. Lett.* **88**, 111116 (2006).
- ⁶Zhao, Q. *et al.* Counting rate enhancements in superconducting nanowire single-photon detectors with improved readout circuits. *Opt. Lett.* **39**, 1869 (2014).

- ⁷Marsili, F., Najafi, F., Herder, C. & Berggren, K. K. Electrothermal simulation of superconducting nanowire avalanche photodetectors. *Appl. Phys. Lett.* **98**, 093507 (2011).
- ⁸Najafi, F., Marsili, F., Dauler, E., Molnar, R. J. & Berggren, K. K. Timing performance of 30-nm-wide superconducting nanowire avalanche photodetectors. *Appl. Phys. Lett.* **100**, 152602 (2012).
- ⁹Heath, R. M. *et al.* Nano-optical observation of cascade switching in a parallel superconducting nanowire single photon detector. *Appl. Phys. Lett.* **104**, 063503 (2014).
- ¹⁰Hu, X., Holzwarth, C. W., Masciarelli, D., Dauler, E. A. & Berggren, K. K. Efficiently coupling light to superconducting nanowire single-photon detectors. *IEEE Trans. Appl. Supercond.* **19**, 336–340 (2009).
- ¹¹Pernice, W. *et al.* High-speed and high-efficiency travelling wave single-photon detectors embedded in nanophotonic circuits. *Nat. Commun.* **3**, 1325 (2012).
- ¹²Akhlaghi, M. K., Schelew, E. & Young, J. F. Waveguide integrated superconducting single-photon detectors implemented as near-perfect absorbers of coherent radiation. *Nat. Commun.* **6**, 8233 (2015).